Supplementary material for "Particle density mobility edge"

In this supplementary material we present additional data and details of the methods used in the main text. First, we show data for additional probes of ETH breakdown such as entanglement entropy. After this we present benchmarks of our time-evolving block decimation simulation of dynamics. Finally, we explore the behavior of the mutual IPR defined in the main text.

I. LOCALIZATION LENGTH AND PARAMETER CHOICE

The dynamics generated by the constrained Hamiltonian, Eq. (1), strongly depends on the choice of the hopping parameters $t_{1,2}$. In order to choose the most suitable parameters for the study of MBME in particle density, we explore localization lengths for a single particle $\xi_{\rm SP}$ and for one pair of particles $\xi_{\rm P}$. These localization lengths are evaluated using ED. We calculate the infinite-time average of the occupation number at each site for an initial state where either a single particle or a single pair are initialized at the first site of the chain. We extract the localization lengths $\xi_{\rm SP}$ ($\xi_{\rm P}$) from an exponential fit of the density curve $\langle n_i \rangle$.

Resulting values of $\xi_{\rm P,SP}$ for fixed $t_1 = 0.5$ and different disorder values and different values of hopping t_2 are shown in Fig. S1. The single particle hopping localization length (dashed line in Fig. S1) does not depend on t_2, and becomes smaller than one lattice spacing for $W \gtrsim 4$. The pair localization length is monotonously increasing with t_2 at fixed value of disorder strength, W. Our aim is to have $\xi_{\rm P}$ in the range between 2 and 5. In this regime, the half-filling case is expected to be delocalized, while at lower densities $\nu \sim 1/5$, when the typical distance between pairs is large, we expect MBL phase. This motivates the choice $t_2 = 2$, since at this value of t_2 $\xi_{\rm P}(W)$ approaches 2 at disorder strength around $W \sim 6$. We note that we avoided further increase of t_2 to keep the model away from the constrained limit: in the case when t_2 dominates over t_1, the model would approximately reduce to a kinematically constrained model that has many disconnected sectors in the Hilbert space.

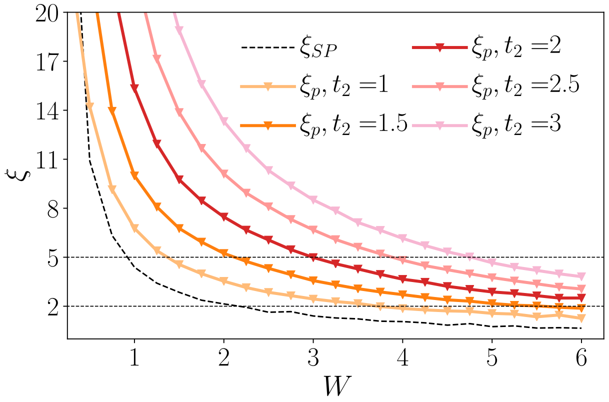

Figure S1. The localization length decreases, as expected, with the disorder strength for all the values of t_2. For every constrained hopping amplitude t_2 it is possible to locate the region of disorder where we expect to see a MBME in particle density as the area among the two dashed lines. As the curve crosses the first dashed line, systems with typical particle spacing 5 will be localized. Nevertheless denser states will still be delocalized, having smaller distance among particles. Data were obtained on a lattice of length $L = 50$ and averaged over 5000 disorder realizations.

In order to rule out the presence of strong finite size effects, we studied the density of state in individual disorder realizations. In the regime when $t_2 \gg t_1$ the strong finite size effects would give rise to the presence of the mini-bands and the DOS would become non-monotonous with numerous peaks corresponding to mini-band structure [30]. Figure S2 confirms that at our choice of parameters even individual disorder realizations have a relatively smooth density of states with Gaussian envelope, thus ruling out the presence of strong finite size effects.

II. ED PROBES OF LOCALIZATION

While in the main text we focused on the two values of filling, $\nu = 1/2$ and $1/5$, here we demonstrate the density dependence of critical disorder. For this purpose we calculate the average ratio of level spacings $r_{\rm av}$ for a single system size $L = 18$ at varying values of density. Fig-

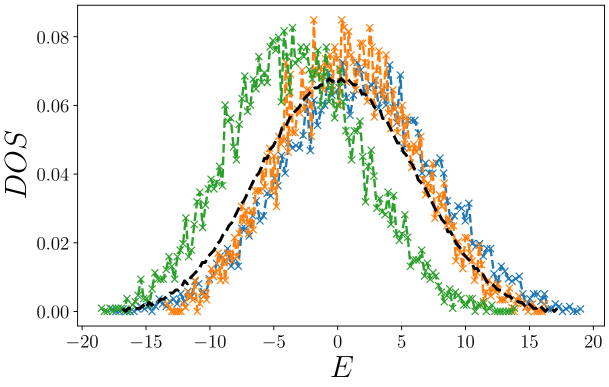

Figure S2. The DOS from single disorder realizations show a relatively smooth behavior and a Gaussian shape, thus confirming the absence of strong finite size effects. DOS refers to a chain with $L = 20$ and $\nu = 1/4$. Disorder strength is $W = 5.0$. Green, blue and orange curves correspond to different disorder realizations, while the black dashed line shows disorder-averaged DOS.

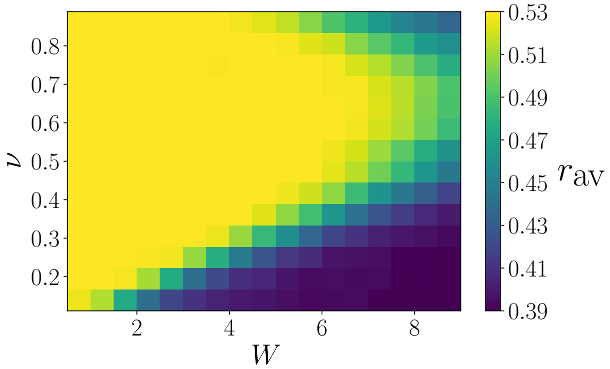

Figure S3. The sharp difference of r_{av} obtained for different ν at the same disorder W clearly shows the MBME in our model. Interestingly, the mobility edge curve $W_c(\nu)$ is not symmetric, but is peaked around $\nu = 2/3$, implying that the states with the maximum number of pairs for fixed size are the hardest to localize. The data is obtained for a system of size $L = 18$, using shift-invert method with $10 - 10^3$ states from the middle of the spectrum and $5 \times 10^4 - 10^3$ disorder realizations.

ure S3 allows to estimate the dependence of the critical disorder on the filling, ν. At low densities ($\nu < \nu_c(W)$) states have r_{av} approaching value characteristic for Poisson distribution of level spacings. In contrast, for dense configurations ($\nu > \nu_c(W)$) the level spacing ratio is close to GOE prediction.

Figure S3 reveals that the most delocalized filling is $\nu = 2/3$, which corresponds to the case when the best packing of pairs in the chain, ●●○●●○· · · , can be achieved. At this filling the Poisson values of r_{av} would be achieved beyond the upper limit of the considered disorder range. Decreasing particle density away from this value causes earlier onset of localization. For instance, fixing disorder value $W = 6.5$ we observe that $\nu = 1/2$ and $\nu = 1/5$ are situated well in delocalized and localized regions.

In addition to the level statistics indicator presented in the main text, we studied other commonly used probes of ergodicity. In particular, Fig. S4 illustrates the behavior of bipartite entanglement entropy for different disorder strengths and different fillings. On the one hand, the finite size scaling of entanglement entropy of eigenstates in the middle of the spectrum shows that for $\nu = 1/5$ and disorder $W > W_c \sim 6$ the entanglement is consistent with area-law. On the other hand, the entanglement of dense systems, $\nu = 1/2$, does not show a similar behavior. The finite size scaling, indeed, shows no crossing at these disorder values, thus suggesting volume-law of entanglement entropy for $\nu = 1/2$.

A. Energy Density MBME

In this section we briefly discuss the presence of many-body mobility edge in energy density in a single density sector of the Hamiltonian Eq. (1). Given the $U(1)$ symmetry, we would expect that a fixed filling sector presents MBME in energy density, similarly to the case of the random field XXZ spin chain. In the middle of the spectrum the density of states is large and eigenstates may remain delocalized, while at the same disorder strength the states at the edges of the many-body spectrum are localized.

To explore the eventual presence of MBME in energy density in the half filling sector, we studied the energy resolved level spacing ratio $r_{\text{Av}}(\epsilon, W)$. The results, dis-

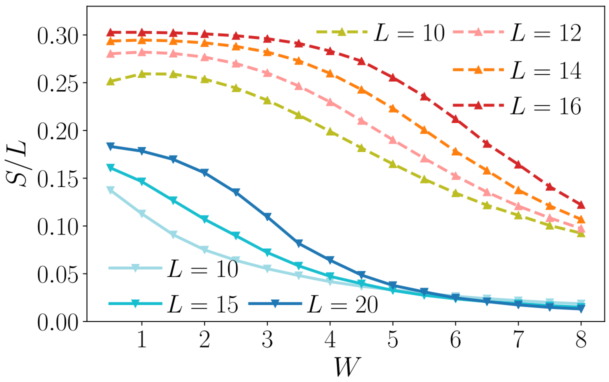

Figure S4. The behavior of half-chain entanglement entropy shows very distinct behavior for dilute (blue-shaded curves) and dense (red-shaded curves) states. The crossing in the dilute states implies that they entered the MBL phase, and thus have area-law entanglement entropy. On the other hand, dense states do not show a similar crossing in this range of disorder, suggesting that they are still in the ergodic phase. The data are obtained with shift-invert method for $10 - 10^3$ eigenstates in the middle of the spectrum and averaged over $5 \times 10^4 - 5 \times 10^3$ disorder realizations.

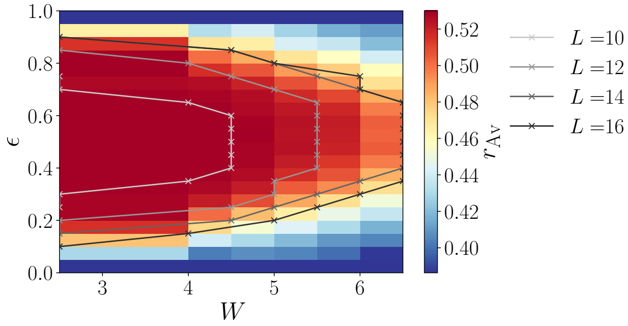

Figure S5. The plot, presenting the energy resolved level spacing ratio for $L = 16$ in the half filling sector, shows clear evidence of MBME. In the center of the band r_{av} approaches the GOE value, while at large and small energy density it is close to the Poisson value. Furthermore, the MBME curves obtained for smaller systems seem to converge at increasing system size, thus suggesting the persistence of the MBME in the thermodynamic limit. The plot was obtained averaging over $n = 10^4,\ 2 \times 10^3,\ 5 \times 10^2,\ 10^2$ disorder realizations for increasing system size from $L = 10$ to $L = 16$.

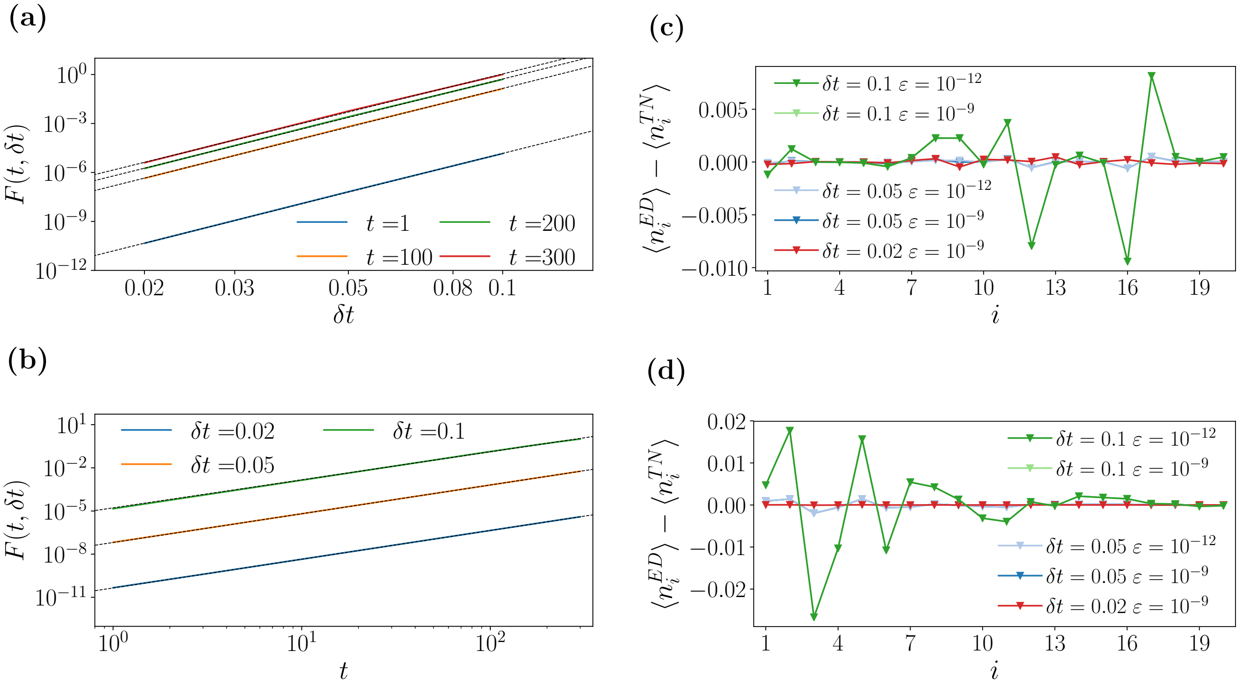

Figure S6. (a-b) Deviation of ground state fidelity from 1 in Trotter time evolution, $F(t, \delta t)$, shows power-law behavior both in time and in time-step, as expected. The data is obtained at density $\nu = 1/5$, system size $L = 20$ and disorder $W = 6.5$ for a particular disorder realization. The plots for other disorder realizations are qualitatively similar. (c-d) The comparison between ED and TEBD time evolution reveals that the most effective way to increase accuracy of TEBD is to decrease the time-step δt. Indeed, the change in the truncation between $\varepsilon = 10^{-9}$ and $\varepsilon = 10^{-12}$ does not have much effect on the the difference between density profiles of exact diagonalization and TEBD. At the same time, the decrease of time step brings the local density profile closer to ED results. The density profiles are calculated by propagating uniform density wave (c) and uniform pair-density wave (d) initial states to time $t = 500$ for a particular disorder realization with $L = 20$, $\nu = 1/5$, $W = 6.5$.

played in figure S5, show evidence of many-body mobility edge; the level spacing ratio, as a function of the energy density $\epsilon = \frac{E - E_{\min}}{E_{\max} - E_{\min}}$, where $E_{\min}$ and $E_{\max}$ are the ground state and the most excited state respectively, increases from the Poisson to the GOE value as ϵ goes from the lower edge to the center of the spectrum and decreases again from the center to the upper edge. This variation is such that at a fixed disorder strength the low and high energy states are localized, while the center of the band is delocalized, thus defining a many-body mobility edge. The scaling of the MBME curves for different system size shows signs of convergence, suggesting stability of the MBME in the thermodynamic limit.

III. MPS SIMULATIONS OF QUENCH DYNAMICS

In our MPS simulation, we time evolve dilute states in large systems $L \geq 30$ up to time $T_{\max} = 500$. For this we use the time-evolving block decimation (TEBD) algorithm with a fourth-order Trotter evolution based on the ITensor library [34]. The main parameter involved in the time evolution algorithm is the time step δt used to split the unitary evolution into a sequence of gates. The error related to the finite size of the time step in the p-th order Trotter expansion grows as δt^p. The other source of error is the finite cutoff, ε, that governs the truncation of singular values in the singular value decomposition (SVD).

While the instantaneous errors related to the truncation and finite time step are known, understanding the propagation of these errors with time and their possible interference is challenging. First we tested TEBD algorithm by evolving the ground state of the same model. Provided that the time evolution is numerically exact, the overlap between the TEBD-evolved ground state, $|\psi_0(t)\rangle = U^{\mathrm{TEBD}}(t)\,|GS\rangle$ and the exact time evolution of the ground state, $|GS(t)\rangle = e^{-\imath E_0 t}\,|GS\rangle$, is supposed to give the identity $\langle \psi_0(t)|GS(t)\rangle = 1$ at all times. For the fourth-order Trotterization the behavior of $F = 1 - |\,\langle \psi_0(t)|GS(t)\rangle\,|$ is known to be proportional to $(\delta t)^8$. The numerical results plotted in Fig. S6(a), confirm these expectations.

Next, we performed a benchmarking of TEBD algorithm against ED time evolution for several disorder realizations and simulation parameters. An illustration of such benchmarking is shown in Fig. S6(c) and (d). In particular, we observed that time step $\delta t = 0.05$ and cutoff $\varepsilon = 10^{-9}$ result in a good agreement between ED and TEBD dynamics. Smaller values of $\delta t, \varepsilon$ would improve

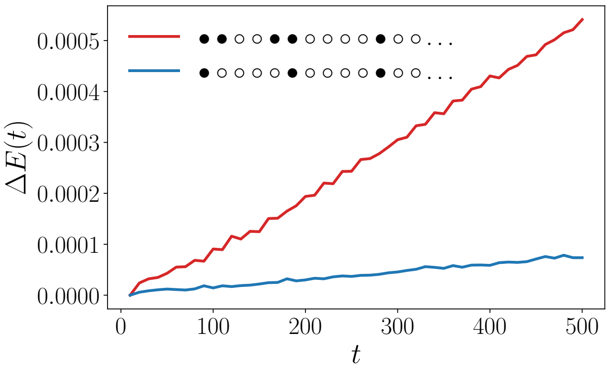

Figure S7. The normalized absolute value of the energy difference from the initial energy $\Delta E(t) = |\langle H(t)\rangle - E(0)|/|E(0)|$ remains very small for both the density wave, blue curve, and the non-uniform, red curve, configurations, confirming the good accuracy of our numerical simulations beyond the ED benchmark. The larger deviation displayed by the non-uniform configuration is understood as a result of the presence of the bubble in the lattice, that increases entanglement growth. The results here shown are obtained averaging over 100 disorder realizations, for the system sizes, $L = 30$, and initial states described in the main text.

the agreement but would result in a dramatic slowdown of the evolution time. Therefore, we decided to use these parameters in the simulations presented in the main text.

When larger system sizes are involved, as it is the case for the simulations actually used in the main text, comparison with exact results is not available. Therefore, other indicators for the accuracy must be studied. Among these, energy conservation through the time evolution is a straightforward probe. The energy deviation $\Delta E(t) = |E(0) - E(t)|/E(0)$, where $E(t) = \langle\psi(t)|\,\hat{H}\,|\psi(t)\rangle$, allows to control the propagation of the error during the Trotter time evolution. In Fig. S7 we show the results for $\Delta E(t)$ in the two quenches presented in the main text, for $L = 30$. The two plots highlight that the average energy deviation is very small in both configurations. In spite of that, a clear difference can be observed among the two quenches, noticing that the non-uniform state has larger error. This is probably due to the enhanced entanglement caused by the presence of the bubble in the lattice. Nevertheless, $\Delta E(t)$ remains very small even at long times, thus confirming the reliability of our long-time numerical simulations.

In all the simulations performed using ITensor [34], we used the $U(1)$ symmetry implementation. In particular, to obtain the numerical results presented in Fig. 2(a) and (d) we set the maximum bond dimension to be 500 and 3000 respectively. As the histograms in Fig. S8 show, all the disorder realizations remained well below the maximum threshold. This fact ensures that we have a control on the error encountered in the evolution, in contrast to time evolution with TDVP with fixed bond dimension, where error estimation is more challenging [51].

IV. ADDITIONAL RESULTS FROM QUENCH DYNAMICS

In the main text we discussed dynamics in quenches that begin from a uniform state or a bubble joined to a more dilute remainder. Below we present details for the quenches in presence of bubble. In addition, we discuss the dynamics resulting from the initial state containing density wave of particle pairs.

A. Pair density and entanglement dynamics in presence of a bubble

Since particle pairs are the most mobile objects, we consider the pair density in quenches that are initialized with the bubble (see Fig. 2(d),(g) in the main text). The pair density is of special interest in these quenches as in Ref. [18] suggested that the instability of the system is ascribed to the ability of the bubble to move. In our model the bubble consists of several pairs, thus motion of the bubble throughout the system would imply the spreading of pairs.

The pair density defined as $\langle n_i n_{i+1}\rangle$ measured at late or infinite times is shown in Fig. S9. In the dense case the late time pair density profile supports delocalization: at late times the density of pairs becomes homogeneous throughout the formerly more dilute region of the system. We note, that the pair density is not a conserved quantity, and it can increase in the process of unitary dynamics.

In contrast, for the dilute case the pair density profile has a pronounced exponential tail away from the initial ergodic region. This shows that pairs spreading away from the initial bubble do not delocalize when encountering additional particles on their way. Indeed, while the late time pair density profile has small peaks around the initial position of particles, these peaks are not very pronounced. In addition, the study of the pair density profile

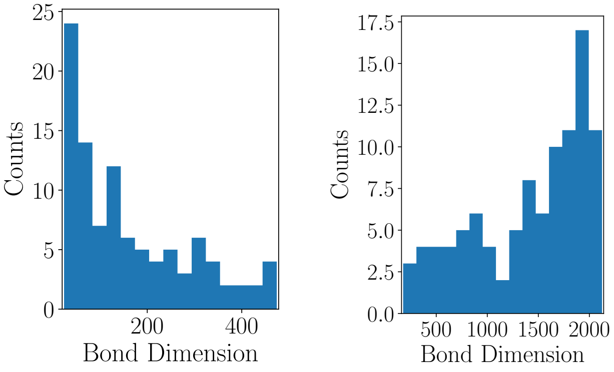

Figure S8. The histogram representing the maximum bond dimension of different disorder realizations show that the threshold values of 500 and 3000 for the uniform density wave (left) and bubble states (right) were never saturated in our simulations.

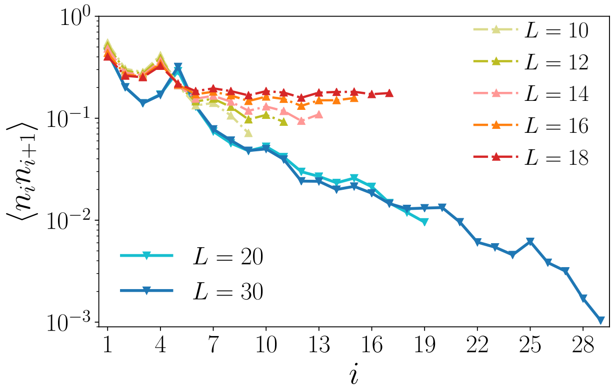

Figure S9. The finite size scaling of the pair density $\langle n_i n_{i+1} \rangle$ shows opposite trend for the dense and dilute cases. The red-shaded curves represent $\nu = 1/2$ configurations: increasing the system size (from yellow to dark red) the pair density becomes more uniform and approaches the thermal value, hence in the thermodynamic limit the probability of finding a pair far from the bubble is almost the same as finding it in the bubble. On the contrary, blue curves ($\nu = 1/5$) show exponential vanishing of the pair density and, furhtermore, increasing system size (from light blue to dark blue) the density decreases, suggesting that at the thermodynamic limit there will be no pair outside the thermal region. Data were obtained with ED, Krylov ($T_{\max} = 1000$) and TEBD ($T_{\max} = 500$) algorithms averaging over 100 disorder samples for the largest MPS simulations ($L = 20, 30$), $3 \times 10^4, 10^4, 5 \times 10^3$ and 10^3 for ED (from $L = 10$ to $L = 16$) and over 10^3 for Krylov algorithm ($L = 18$).

in the uniform density wave at $\nu = 1/5$ reveals an almost constant behavior, centered around $\langle n_i n_{i+1} \rangle \sim 10^{-3}$, which corresponds to the values reached at the end of the exponential tail in the system with $L = 30$ in Fig. S9.

Next, we focus on understanding different contributions to entanglement growth. Exploiting the $U(1)$ symmetry of our model and following Refs. [38, 39], we split the von Neumann entanglement entropy into a configuration and a particle transport contributions. Indeed, due to conservation of the total number of bosons the full reduced density matrix ρ must have a block-diagonal form. Individual blocks within ρ can be written as $p_n \rho^{(n)}$, where p_n gives the probability to have n particles in the susbsystem A and $\rho^{(n)}$ is normalized as $\operatorname{tr} \rho^{(n)} = 1$. Using such representation of the reduced density matrix we can split the full entropy into $S_{vN} = S_C + S_n$ as:

$$\begin{aligned} S_{vN} &= -\operatorname{tr} \rho \log \rho = -\sum_n p_n \operatorname{tr} \rho^{(n)} \log\left(p_n \rho^{(n)}\right) \\ &= -\sum_n p_n \log p_n - \sum_n p_n \operatorname{tr} \rho^{(n)} \log \rho^{(n)} \qquad \text{(S1)} \\ &= S_n + S_C . \end{aligned}$$

In this way the entanglement growth is split into two contributions: one coming from the particle transport, and another originating from dephasing between different configurations with the same particle number. Interestingly, Fig. S10 shows that while the overall entanglement entropy grows faster than logarithmic, this is due only to the configuration part (yellow curve) and the entanglement due to particle transport has logarithmic growth. The logarithmic growth of S_n is consistent with the logarithmic particle transport presented in Fig. 2(h) in the main text and with other transport measures presented in the next section. We identify this behavior as a hallmark of MBME, and note that it happens on long, yet experimentally accessible timescales $t \sim 50(\hbar/t_1)$.

Recent work [40] demonstrated that the logarithmic

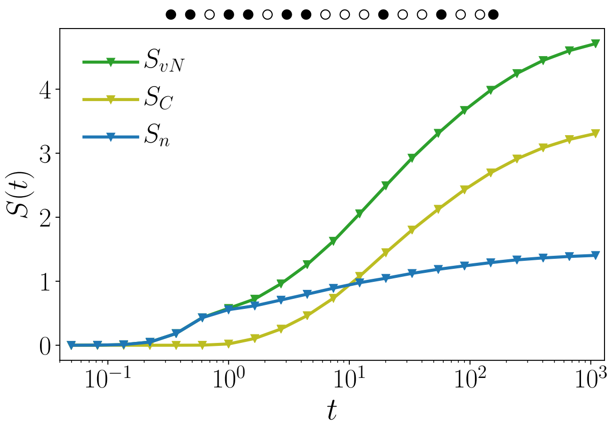

Figure S10. The different contributions to the entanglement entropy of the bubble show that the overall behavior of the von Neumann entropy is faster than logarithmic. Nevertheless this behavior can be ascribed to the sole configurational entropy S_C, while the particle transport contributes to the purely logarithmic growth. The curves are obtained through Krylov evolution up to $T_{\max} = 1000$ averaged over 1000 disorder realizations for $L = 18$ and $W = 6.5$.

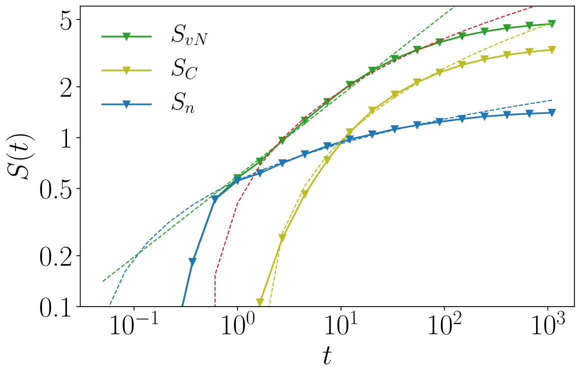

Figure S11. The log-log plot of the entropies discussed in Eq. (S1) confirms that only the total entropy is growing as a power-law, while both S_n and S_c grow slower. In particular, S_n grows as a first degree polynomial in $\log(t)$ (dashed green line) and S_C as a second degree polynomial in $\log(t)$ (orange dashed line). The sum of these two behaviors (red dashed line) agrees with the power-law behavior (dashed blue line).

growth of the number entropy is expected in the thermal phase, provided there is particle transport over distances that increase as a power-law in time, $l \propto t^{\nu}$. [1] The authors also predict a power-law scaling of the configuration entropy, which we do not observe, as shown in figure S11. We attribute the slower than power-law growth of configuration entanglement to the localized nature of the right half of the chain, which in turn reduces the number of possible configurations until the particle transport from the left half leads to delocalization.

Further analysis of the entanglement dynamics shows that S_{vN} grows in a power-law fashion $S_{vN} \approx at^{b}$, corresponding to the dashed blue fit in Fig. S11, over a relevant time interval. On the other hand, both S_n and S_c behave as polynomials in $\log(t)$, of first and second degree respectively, and their sum (dashed red line) reasonably approximates the power-law behavior of S_{vN}, as one can expand $t^b \approx 1 + b\log(t) + \frac{b^2}{2}\log^2(t)$.

Finally, to support our interpretation of logarithmic increase of S_n as due to transport, we study the dynamics of density correlation functions and fluctuations. Figure S12 presents the dynamics of connected correlation functions $C(i,t) = \langle \hat{n}_i \hat{n}_{L/2}\rangle - \langle \hat{n}_i\rangle\langle \hat{n}_{L/2}\rangle$ with respect to the central site of the chain, the local density fluctuations $\delta n_i = \langle \hat{n}_i^2\rangle - \langle \hat{n}_i\rangle^2$ and the density fluctuations in the dilute part of the chain $\delta n_R = \langle \hat{n}_R^2\rangle - \langle \hat{n}_R\rangle^2$, where $\hat{n}_R = \sum_{i=L/2}^{L} \hat{n}_i$. The logarithmic dynamics of these quantities is consistent with the behavior of number entropy, thus proving the further support for the existence of slow transport in the dilute part of the chain.

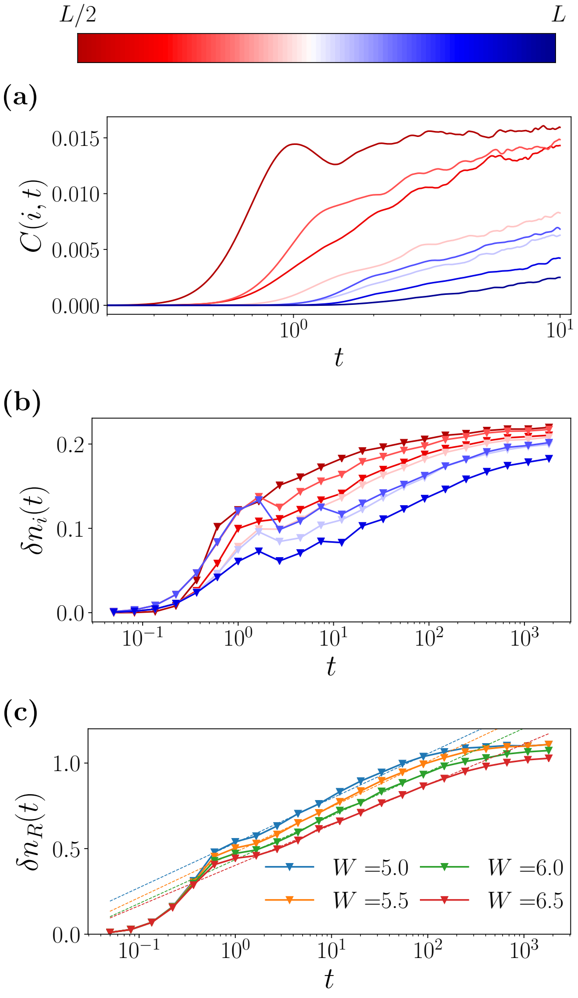

Figure S12. Time dynamics of correlation functions (a), local density fluctuations (b) and density fluctuations in the dilute half of the chain (c) all show, after an initial power-law growth, logarithmic increase with time. In particular, correlations far away from the central site (blue curves, as encoded in the legend above) show signs of a logarithmic light-cone. Similarly, local density fluctuations deep in the localized region present slower dynamics. Finally, panel (c) shows how increasing disorder slows the growth of the global density fluctuation of the dilute half. These results were obtained with the Krylov method on system size $L = 18$ for $W = 6.5$ (a), with ED on system size $L = 16$ and $W = 6.5$ (b) and for different disorder values (c), averaging over 200 disorder realizations.

B. Quench dynamics from a pair density wave state

Below we consider quench from a pair-density wave of period $2/\nu$. These configurations accommodate the maximal possible number of pairs in the uniform state. Figure S13 confirms that such state is localized at $\nu = 1/5$ and is relaxing in the dense case. Dense systems display strong dependence on the system size and increased tendency towards relaxation at larger system sizes, L. In contrast, at $\nu = 1/5$ the late time density profile has almost no dependence on the size of the system. In particular, even at very large lengths the curves do not approach the average density represented by the dashed black line.

V. $\mathcal{P}$ AS A FUNCTION OF BUBBLE DISTANCE

In the text we introduced a quantity $\mathcal{P}(|\psi_1\rangle, |\psi_2\rangle)$ that measures how similar the expansion of $\psi_{1,2}$ over eigenstates is. We birefly mentioned that the case where $|\psi_1\rangle = |\psi_2\rangle$ corresponds to the usual participation ratio, hence we refer to the inverse of $\mathcal{P}$ as mutual inverse participation ratio (mIPR). The mutual IPR assumes very different values depending on the nature of the two states: values of mIPR $O(\mathcal{N})$ correspond to two vectors that

---

[1] We note, that although the authors of Ref. [40] report unbounded growth of the number entanglement in the MBL phase, the successive work of Luitz and Bar Lev [41] shows that this is due to rare particle fluctuations around the boundary between the two subsystems and the growth disappears at large enough system size.

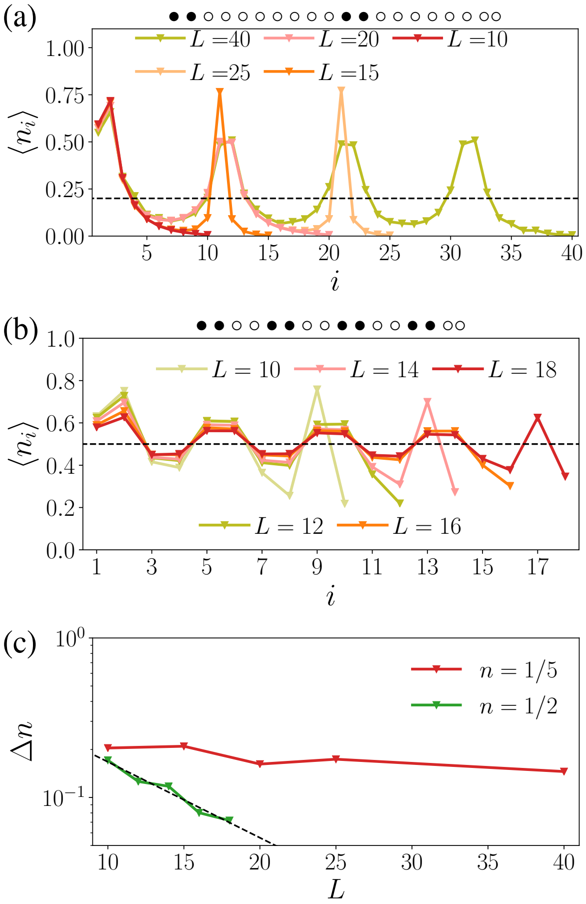

Figure S13. The late time density profiles of the pair density waves at dense, $\nu = 1/2$, and dilute, $\nu = 1/5$, fillings show very different behavior. (a) Dilute configurations are essentially frozen, and do not approach the thermal density represented by the black dashed line. (b) In contrast, at $\nu = 1/2$ relaxation is enhanced at larger L. (c) The deviation of late time density from the thermal value decay exponentially with system size as $e^{-L/\xi_T^{\text{pair}}}$ with $\xi_T^{\text{pair}} \approx 8.1$. In contrast for $\nu = 1/5$, the residual density remains nearly constant with system size and naïve fit to the exponential gives an order of magnitude larger scale, $\xi_T^{\text{dilute}} \approx 84$. Data at $\nu = 1/5$ is obtained via ED ($L = 10$, $L = 15$, and $L = 20$ with 5×10^4, 10^4, and 2×10^3 disorder realizations), Krylov time evolution ($L = 25$, $T_{\max} = 10^3$ and 10^3 disorder realizations) and TEBD ($L = 40$, $T_{\max} = 300$ and 100 disorder realizations). For $\nu = 1/2$ we used ED ($L = 10$, 12, 14, and 16 with 3×10^4, 10^4, 5×10^3, and 10^3 disorder realizations) and Krylov time evolution ($L = 18$, $T_{\max} = 10^3$, and 10^3 disorder realizations).

have similar expansion over eigenstates, while very large values of mIPR imply that the expansion is very different. In the main text we analyzed the mIPR between two product states where the bubble is located at the left and right end of the system respectively, see Eqs (2)-(3). Such pair of states corresponds to the maximum possible displacement of the bubble in the chain. Below we illustrate the behavior of mIPR between pair of states which correspond to a smaller bubble displacement.

In our analysis we measure the mIPR, $\mathcal{P}_d^{-1} = \mathcal{P}^{-1}(\psi_L, \psi_d)$, between the following states in the dense limit (half-filling, $L = 12$),

$$|\psi_L\rangle = \boxed{\bullet\bullet\bullet\bullet\bullet\bullet}\,\circ\circ\circ\circ\circ\circ, \tag{S2}$$

$$|\psi_d\rangle = \underbrace{\circ\circ\circ}_{d}\boxed{\bullet\bullet\bullet\bullet\bullet\bullet}\,\circ\circ\circ\,. \tag{S3}$$

Here we use the bubble that contains all particles to maximize the range of achievable displacements. For the dilute case, $L = 15$, we use similar pair of states with bubble containing 3 particles ($\nu = 1/5$).

In the thermal phase, eigenstates are approximately given by random vectors in the Hilbert space and their average overlap with other normalized vectors approaches the value predicted by random matrix theory, irrespective of the state or the eigenstate. In the weak disorder limit, we then expect $\mathcal{P}_d^{-1}$ to be independent on the distance between the two bubbles and to have the same behavior as the conventional IPR: $\mathcal{P}_d^{-1} \sim \mathcal{N}$. This expectation is confirmed by the results presented in fig. S14(a) and (b) for $W = 0.5$.

On the other hand, in the MBL phase eigenstates are not similar to random vectors, but instead are characterized by a set of local integrals of motion that have a finite overlap with the local particle density. Thus, two product states with globally different arrangement of particles are expected to have drastically different expansion over eigenstates. Therefore, we expect $\mathcal{P}_d^{-1} \propto \exp[d/\xi]$. As presented in figure S14(a) and (b), at strong disorder our results support this hypothesis for both dilute (a) and dense (b) states.

At intermediate disorder strength, we observe a qualitative difference between dense and dilute cases. Dilute configurations, Fig. S14(a), show exponential behavior already at $W = 4.5$, whereas dense states in Fig. S14(b) need much stronger disorder to clearly present the same trend. This result confirms the presence of mobility edge and is consistent with the observed absence of pair spreading reported in Figure S9 and also with the finite size scaling of mIPRs shown in the main text, Fig. 3.

VI. DYNAMICAL PROBE OF THE ABSENCE OF RESONANCES

The discussion on mutual IPR showed how tunneling processes are strongly suppressed in the dilute case of our model. In addition to eigenstates analysis, we also studied long time dynamics of states with a thermal bubble. In this way, it was possible to verify whether a bubble initialized at a certain position can dynamically give rise to a dense region somewhere else in the chain. In order to study this process we defined a projector onto the subset of Hilbert space that has large density in a certain region.

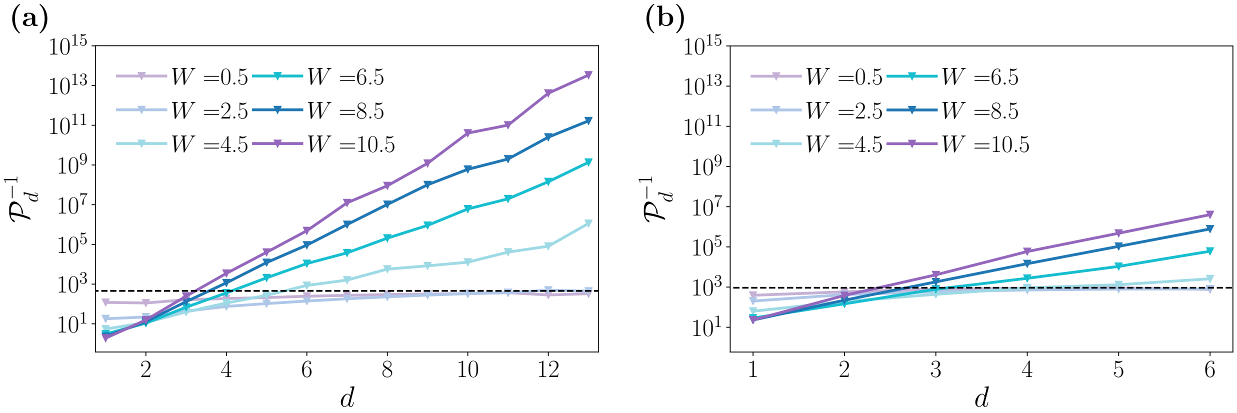

Figure S14. The mutual IPR, $\mathcal{I}_d$, that quantifies the inverse probability of bubble tunneling d sites, increases exponentially with d at strong disorder. At weak disorder the mIPR approaches the Hilbert space dimension, $\mathcal{N}$, shown by a dashed line. In the dilute system in (b), $W = 4.5$ marks the onset of the exponential growth, suggesting that the thermal bubble is frozen at its initial position. On the other hand, for $\nu = 1/2$, in (a), the clear exponential behavior emerges only at larger disorder. $\mathcal{I}_d$ was calculated for system sizes $L = 15$ and $L = 12$ in dilute and dense case respectively and averaged over 10^4 disorder realizations.

More specifically, we define

$$\hat{P}_{\nu_c}(L_0, i) = \sum_{|\phi_\alpha\rangle \in \mathcal{C}} |\phi_\alpha\rangle \langle \phi_\alpha| \,, \tag{S4}$$

where states $|\phi\rangle$ are all possible product states that satisfy the condition $\nu \geq \nu_c$ in the region $[i, i + L_0]$. This projector selects all configurations where the system is locally above the mobility edge. We notice that $\hat{P}_{\nu_c}(L_0, i)$ takes into account all possible configurations, thus considering also the entropic factor.

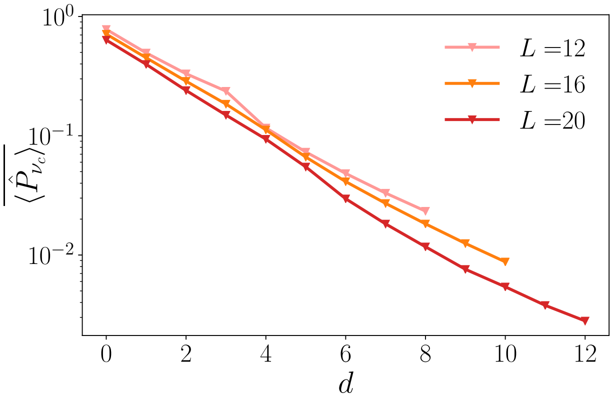

Figure S15. The late time evolution of $\overline{\langle P_{n_c}(L_0, d)\rangle}$ shows exponential decay for all the system sizes studied ($L = 12, 16, 20$ at density $\nu = 1/4$). Furthermore, we notice that increasing the system size the exponential vanishing becomes more severe, suggesting that in the thermodynamic limit there would be no motion of the bubble at all. These results were obtained using $10^4, 5 \times 10^3$ and 10^3 disorder realizations for the system sizes from smaller to larger.

In order to understand what is the minimal required size of the region L_0, we use the lengthscale extracted from the decay of Δn. Fit in Fig. 2(c) in the main text yields $L_0 \simeq 6 \div 7$, while fit in Fig. S13(c) gives a somewhat larger scale. We define an initial state $|\psi_0\rangle$ that has an entangled dense region of size approximately L_0 (described by a linear superposition of product states $|\phi_i\rangle$) followed by a product state:

$$|\psi_0\rangle = \frac{1}{\sqrt{N_{\mathcal{C}}}} \sum_{i=1}^{N_{\mathcal{C}}} |\phi_i\rangle \otimes |\circ\circ\circ\bullet\circ\circ\rangle \,. \tag{S5}$$

Below, we fix the overall density to $\nu = 1/4$ and $W = 6.5$, which still corresponds to a localized system. The dense region is obtained as a superposition of different configurations with $N - 1$ particles in $L_0 = 2(N - 1)$ sites. The remaining particle is initialized in the middle of the last segment of the chain. For instance, for $L = 16$ this results into following initial state:

$$\begin{aligned} |\psi_0\rangle = \frac{1}{\sqrt{N_{\mathcal{C}}}} \Big[& \boxed{\bullet\bullet\circ\bullet\circ\circ}\,\circ\circ\circ\circ\bullet\circ\circ\circ\circ\circ\circ + \\ & \boxed{\bullet\circ\bullet\circ\bullet\circ}\,\circ\circ\circ\circ\bullet\circ\circ\circ\circ\circ\circ + \\ & \boxed{\bullet\bullet\circ\circ\bullet\circ}\,\circ\circ\circ\circ\bullet\circ\circ\circ\circ\circ\circ \; + \ldots \Big], \end{aligned} \tag{S6}$$

where the boxed area contains a dense entangled bubble and the remainder is in the dilute state.

The initial state $|\psi_0\rangle$ is then evolved through the Hamiltonian (1) in a quench protocol. After time evolution up to a maximum time $T_{\max} = 1000$, we measure $\langle P_{\nu_c}(L_0, d)\rangle = \langle \psi(t)| \hat{P}_{\nu_c}(L_0, d) |\psi(t)\rangle$, which quantifies the probability of encountering a bubble shifted by d sites from the initial position of the bubble.

Finally, averaging over all different product states in the dilute part of the chain and over disorder we obtain the data in Fig. S15. This plot reveals that the probability of having a dense ($\nu > \nu_c$) region decays exponentially with the distance d from its initial location. This is in agreement with our long-time TEBD dynamics, Fig. S9, that reveals localization of individual pairs. Thus, we conclude that bubble does not spread resonantly but rather tunnels throughout the system. Moreover, the finite size scaling analysis shows that increasing the system size the decay of $\overline{\langle P_{\nu_c}(L_0, d)\rangle}$ with distance d is enhanced. Therefore in the dilute regime of our model the bubble remains localized around its initial position.

---

[41] David J. Luitz, and Yevgeny Bar Lev "Is there slow particle transport in the MBL phase?," arXiv e-prints , arXiv:2007.13767 (2020), arXiv:2007.13767 [cond-mat.dis-nn].